Ion energy distributions and optical emission spectra in NF_3-based process chamber cleaning plasmas

Hsin-Pai Hsueh and Robert T. McGrath[a)]
Electronic Materials and Processing Research Laboratory, Materials Research Institute, The Pennsylvania State University, University Park, Pennsylvania 16802

Bing Ji, Brian S. Felker, John G. Langan,[b)] and Eugene J. Karwacki
Air Products and Chemicals, Inc., 7201 Hamilton Boulevard, Allentown, Pennsylvania 18195

(Received 11 August 2000; accepted 23 April 2001)

To minimize ion bombardment induced damage in NF_3-based chamber cleaning plasmas, we have studied the effects of diluent gases and reactor pressure on ion energy distribution functions in NF_3 plasmas. We have utilized plasma ion mass spectrometry, ion energy analysis, and optical emission spectroscopy in 25 mol % NF_3 plasmas with argon, helium, and oxygen diluents. We have also compared the NF_3-based plasma measurements to those of 50 mol % C_2F_6/O_2 plasmas. We have demonstrated that diluting with helium and operating at higher pressures will reduce ion energies in NF_3 plasmas while maintaining superior chamber cleaning performance. In addition, we have correlated the intensity ratio of specific argon emission lines to average ion energies at the grounded electrode. This correlation provides a practical diagnostics tool for further optimization work.
© *2001 American Vacuum Society.* [DOI: 10.1116/1.1379794]

I. INTRODUCTION

NF_3 or fluorocarbon-based plasmas are widely used to clean plasma-enhanced chemical-vapor deposition (PECVD) process chambers. Compared with fluorocarbon-based plasmas, NF_3 offers advantages of shorter atmospheric lifetime, avoidance of fluorocarbon contamination residues, maximized PECVD tool availability resulting from faster etch rates for removal of silicon dioxide and silicon nitride residues on the interior surfaces of the tools, and further downstream cleaning in the reactor as a result of longer radical lifetimes.[1–4] These advantages of NF_3-based cleaning discharges can be fully realized only if ion bombardment damage to chamber interior components can be simultaneously minimized. Diluent or buffer gases are commonly used to optimize both fluorocarbon- or NF_3-based chamber cleaning process plasmas.[5–10] High etch rates and shorter chamber cleaning times in NF_3-based plasmas have been achieved by using high-pressure (1–3 Torr) and high-power density (0.5–2 W/cm^2).[5,7] While etch-rate-optimized plasmas improve the availability and overall productivity of PECVD tools, gradual hardware degradation over time may occur due to bombardment by large fluxes of high-energy ions. Results presented show that through proper choice of diluent gas, power density, and pressure, ion energies incident upon process chamber electrodes can be minimized, thereby minimizing hardware damage during chamber cleaning, while simultaneously maintaining sufficiently high etch rates. In this work, we directly measured energy distributions of positive ions incident upon the ground electrode in chamber cleaning plasmas. We simultaneously measured optical emission spectra (OES) and have correlated OES line intensity ratios with observed ion energy distributions and corresponding etch rates.

The objectives of this investigation were: (1) to study the effects of diluent gas and pressure on ion concentrations and ion energy distributions; and (2) to ascertain if a correlation could be established between the ion measurements and features in the OES. Knowledge obtained in this study offers some practical guidance for reduction of hardware damage while minimizing process chamber cleaning times. We chose to operate our plasma reactor under conditions previously optimized for maximum etch rates.[5] Specifically, 25 mol % NF_3 was used with argon, helium, and oxygen diluents. For comparison, we also made similar measurements in 50 mol % C_2F_6 in C_2F_6/O_2 plasmas.

II. EXPERIMENT

We carried out the measurements in an ultra-high-vacuum compatible, capacitively coupled plasma reactor. Figure 1 is the schematic diagram of the setup. The plasma reactor has been described in detail in previous optimization work.[5] The diameter of the upper electrode is 3 in. while that of the lower electrode is 3.5 in. The electrode spacing was fixed at 1 in. for all of the measurements reported here. The upper electrode was driven at 13.56 MHz. The lower electrode and the chamber wall were grounded. Both electrodes were water cooled at 25 °C inlet temperature. In all measurements, the output of the rf generator (RF Power Products RF-10) was set at 60 W. The matching network (ENI MW-5) was manually tuned to minimize the reflected power.

An ion energy analyzer/quadrupole mass spectrometer (Hiden Analytical, Inc., EQP-300) was used to measure relative ion concentrations and ion energy distributions. As shown in Fig. 1, the EQP probe was mounted beneath the grounded lower electrode. Ions enter the EQP probe through a 30-μm-diam orifice made of a piece of thin stainless-steel foil. The foil and the grounded lower electrode were in electrical contact to ensure that they were at the same potential when the plasma was running. The 30-μm-diam orifice is

[a)]Electronic mail: mcgrath@psu.edu
[b)]Current affiliation: Novellus Systems, Inc., San Jose, CA 95054.

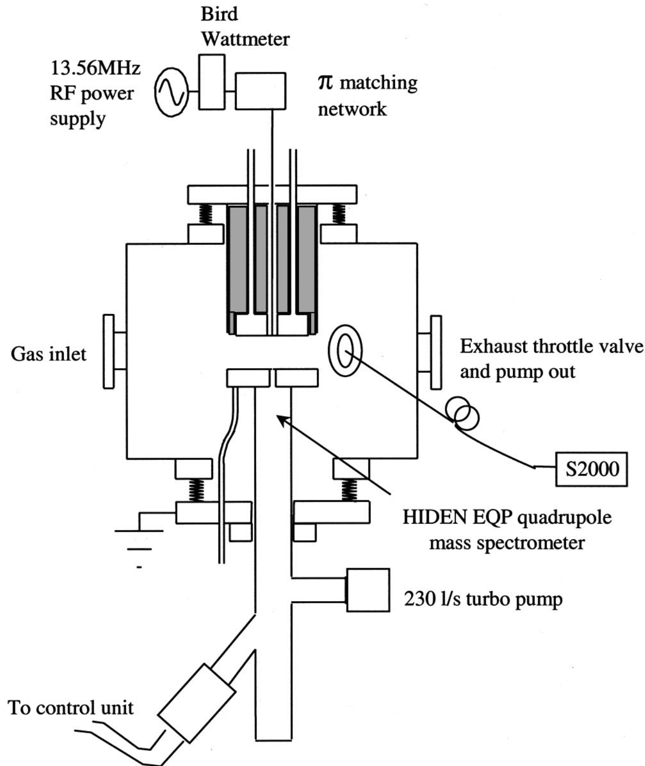

FIG. 1. Schematic diagram of the capacitively coupled process research reactor. The Hiden EQP mass spectrometer was mounted beneath the grounded lower electrode.

sufficiently small so as not to perturb the local structure of the plasma sheath. No extraction voltage was applied to sample the ions from the plasma. As ions drift from the bulk plasma into the sheath, they are accelerated by the electric field across the sheath, pass through the sampling orifice, and enter the EQP probe analysis chamber. The EQP probe was differentially pumped by a 230 l/s turbomolecular pump. The probe interior pressure was maintained below 5×10^{-6} Torr for all measurements. At this pressure, neutral atom and molecule mean-free paths are approximately 1 m. Thus, gas collisions and recycling within the probe are minimized. In contrast to more conventional neutral gas mass spectrometry, no probing analysis electron beam was required for these measurements. Instead, the incident ion fluxes were directly analyzed to determine the ion energy distribution functions (IEDFs) and relative concentrations of each ionic species present.

A fiber-optic spectrometer (Ocean Optics, Inc., S2000) mounted onto a side view port was used to record the optical emissions. Spectra were recorded in the wavelength range of 200–875 nm with 0.5 nm resolution. A blackbody light source was used to correct for the wavelength-dependent transmission efficiencies of the window, the fiber, and the spectrometer. Only corrected OES line intensities were used in the analysis presented. The OES and the ion energy distributions were measured simultaneously for each set of discharge conditions.

III. RESULTS AND DISCUSSIONS

A. Survey of relative ion concentrations

The first three data columns in Fig. 2 show fractional composition of the incident ion fluxes at the grounded electrode in 25 mol % NF_3 discharges diluted with argon, helium, and oxygen, respectively, operated at 0.5 Torr and 1.1 W/cm^2 power density. The fourth data column in Fig. 2 shows the corresponding flux composition for a 50 mol % C_2F_6 discharge diluted with O_2 under the same conditions. The flux compositions shown result from integration of the IEDFs that were measured. For each pressure and gas composition, the electrostatic lenses of the EQP were tuned to maximize the intensity of the IEDF signals collected for each ion mass. When operated in the neutral gas analysis mode, the collection efficiency of the EQP is reported to vary with mass. The procedures used for these measurements avoid any collection efficiency mass discriminations associated with collection of ion production within the probe by electron-beam ionization of the neutral gas being analyzed. In addition, no mass transport corrections are required for neutral gas (or ion) analysis of species lighter than 60 amu. Corrections required for species near 80 amu are about 15%

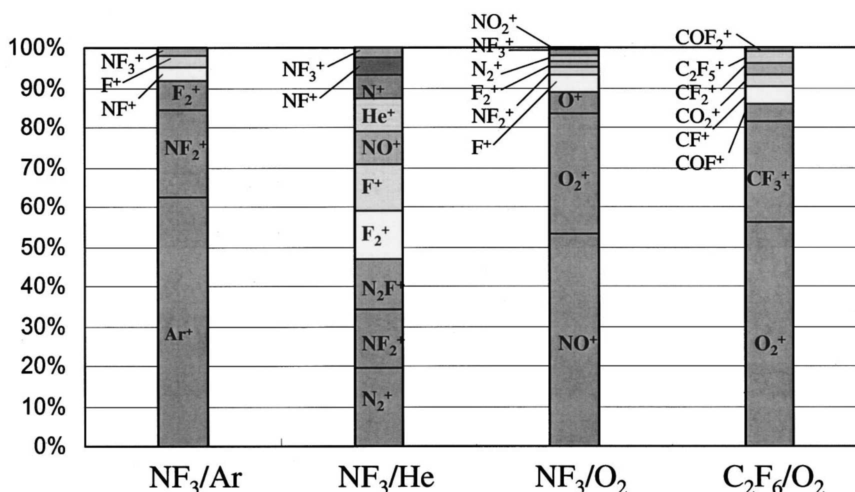

FIG. 2. Fractional composition of the incident ion flux at the grounded electrode: (a) 25 mol % NF_3 in Ar plasma; (b) 25 mol % NF_3 in He plasma; (c) 25 mol % NF_3 in O_2 plasma; and (d) 50 mol % C_2F_6 in O_2 plasma.

for neutral gas analysis and less for the direct collection ion mass analysis executed in this study.[11,12] Since all but one of the ion masses reported in Fig. 2 are below 80 amu, no correction factors for mass discrimination were included.

For all of the gas mixtures studied, power coupling to the plasma varies with pressure. Correspondingly, both optical emission intensities and ion fluxes were observed to vary with pressure. The fractional composition of the incident ion fluxes shown in Fig. 2 also varied somewhat with pressure, reflecting both changes in composition of the bulk plasma as affected by power coupling and changes in sheath collision processes. In the discussion below, the observed flux compositions provide insights into both sheath collisional processes and bulk plasma behavior. The flux compositions shown in Fig. 2 are representative of those observed throughout the pressure ranges where power coupling was good (0.5–2.0 Torr, depending upon gas composition). When power coupling degraded, the fractional abundance of the principal ion or ions was generally observed to drop as the discharge approached extinction.

To understand quantitatively the relative ion concentrations in NF_3 discharges, we need to know the dynamics of electron interaction with NF_3 and its daughter products, and the dynamics of ion–molecule interactions. Most importantly, we need to know the ionization threshold energies and cross sections, the electron-impact fragmentation patterns and yields, and the cross sections for various collisional processes. Unfortunately, only limited data for NF_3 dissociation and dissociative ionization are available. The data for electron collisions with NF_3 fragmentation daughter products are fewer. Tarnovsky *et al.* reported threshold energies of 14 eV for ionization of NF_3 to produce NF_3^+, 15 eV for dissociative ionization of NF_3 to produce NF_2^+, and 23 eV for dissociative ionization of NF_3 to produce NF^+.[13] Reese and Dibeler reported slightly lower values of 13.2, 14.2, and 17.9 eV, respectively, for these thresholds.[14] By filling our chamber with NF_3 gas (no discharge), we were able to use the EQP probe's appearance potential capability to measure the dissociative ionization thresholds for the various NF_3 fragments. We find thresholds for production of NF_3^+, NF_2^+, and NF^+ of 15, 15.5, and 20.5 eV, respectively. The minimum uncertainty of our values is ±0.5 eV, which is the tuning accuracy of the ionizing electron beam in the EQP probe. Our threshold values are in closer agreement with those of Tarnovsky *et al.*, and for convenience of discussion, we have plotted their cross section data in Fig. 3. In addition, we have plotted in Fig. 4 threshold energies for ionization processes and atomic metastable states that are relevant to the data analysis present.

1. Argon as the diluent for NF_3 discharge

As shown in column 1 of Fig. 2, Ar^+ is the most abundant ion in 25 mol % NF_3/Ar plasmas. The high abundance of Ar^+ ions is due to the relatively low ionization potential (IP) and high ionization cross section of argon atoms. Since argon is manifestly electropositive, with each Ar ionization producing an electron, the 40%–45% Ar^+ concentration shown in column 1 of Fig. 2 implies that discharges with 75 mol % argon diluent are less electronegative than the other discharges discussed below. Argon emission line intensities are strongest at a pressure of 0.75 Torr, reflecting the optimal rf power coupling into the discharge and larger electron densities at this pressure. At pressures below 0.2 Torr and above 1.5 Torr, discharges in 25 mol % NF_3/Ar plasmas are difficult to maintain at a fixed input power level of 60 W.

The relative concentrations of NF_x^+ ions, $[NF_x^+]$, are qualitatively consistent with the cross-section data of Tarnovsky *et al.* shown in Fig. 3, i.e., $[NF_2^+]>[NF^+]>[NF_3^+]$. However, $[NF_2^+]$ appears to be much higher than the concentrations of the other two NF_x^+ ions. This may result from additional NF_2^+ production pathways due to NF_3 collisions with Ar^+. Argon has an ionization potential of 15.76 eV, so Ar^+ has sufficient energy to produce NF_2^+ by dissociative ionization. In fact, the reaction of argon ions with NF_3 has been observed to occur at a near gas collisional rate constant,[15]

$$Ar^+ + NF_3 \rightarrow Ar + F + NF_2^+ . \quad (1)$$

Argon metastable states, $3s^2 3p^5 (^2P^\circ_{3/2}) 4s^2 [3/2]_2 (^3P^\circ_2)$ and $3s^2 3p^5 (^2P^\circ_{1/2}) 4s^2 [1/2]_0 (^3P^\circ_0)$, have energies of 11.55 and 11.72 eV, respectively,[16] and therefore, lack sufficient energy to dissociatively ionize NF_3.

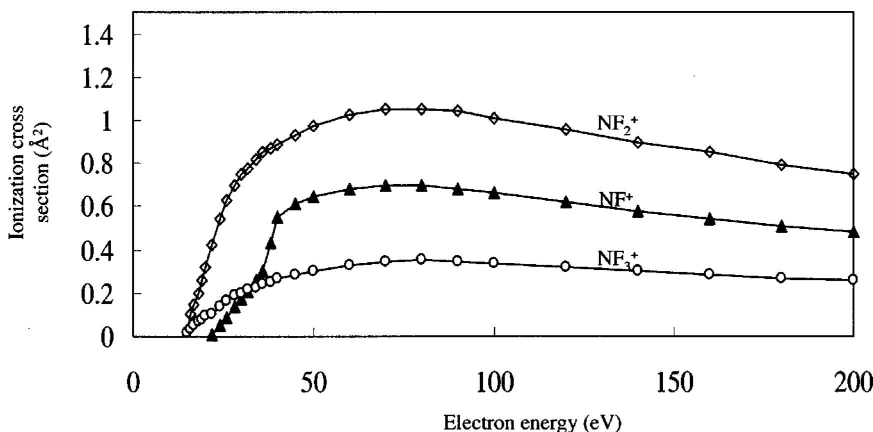

FIG. 3. NF_3 ionization cross sections from Tarnovsky *et al.* (Ref. 13).

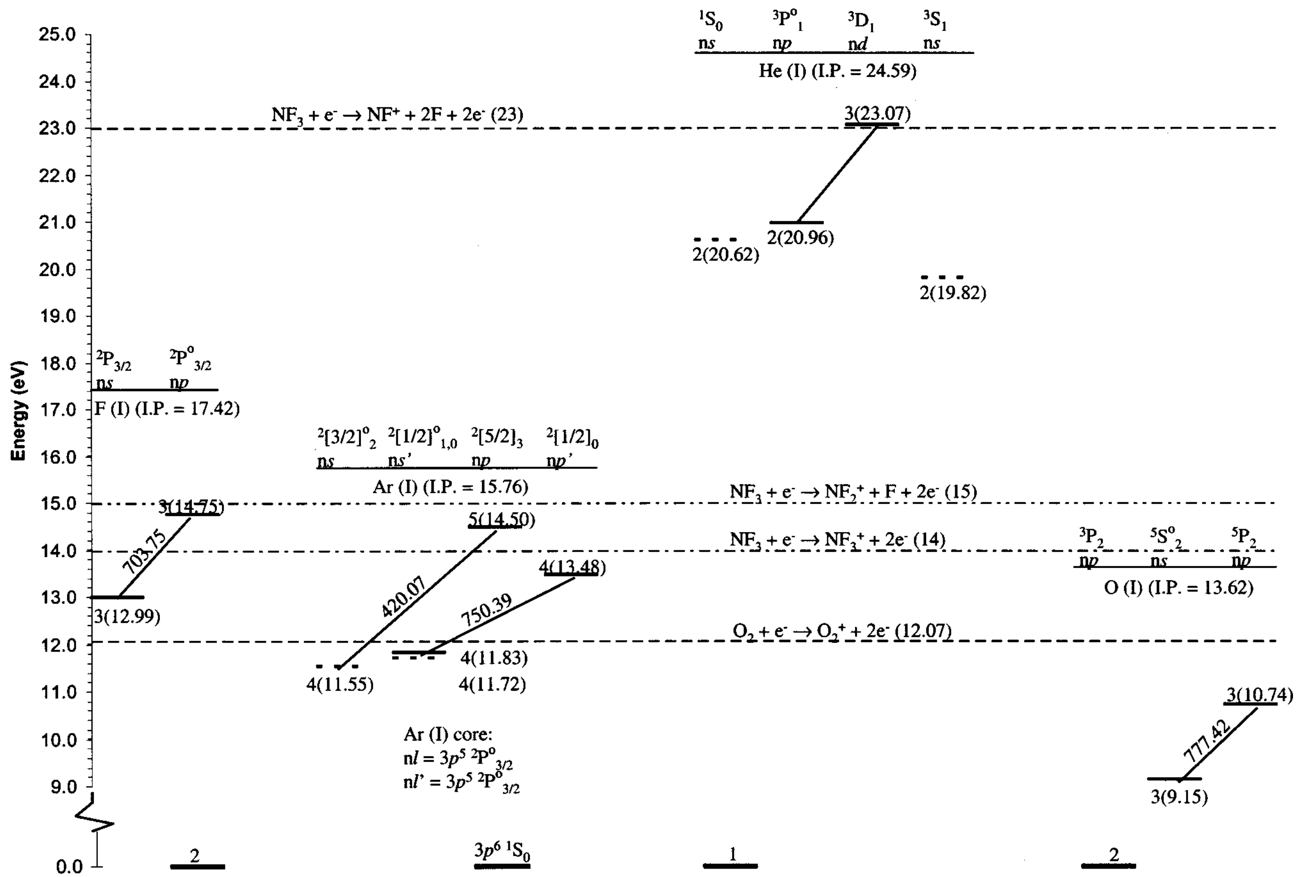

FIG. 4. Selected atomic energy levels and transitions (Grotrian diagrams) for F (I), Ar (I), He (I), and O (I). Level energies shown in parentheses are in eV, and transition wavelengths are in nm. Metastable states are shown in dashed lines. The threshold energies for selected molecular ionization processes are also shown.

Notable concentrations of F_2^+ (11%) and F^+ (4%) are observed in 25 mol % NF_3/Ar plasmas. The F^+ production from dissociative ionization of NF_3 has a threshold energy of 25 eV. The ionization potential of a fluorine atom is 17.42 eV. Although Ar^+ does not have sufficient stored energy to produce F^+ via direct dissociation of NF_3 or direct ionization of fluorine atoms, Ar^+ can produce neutral fluorine atoms via several mechanisms, such as the reaction pathway shown in Eq. (1) above. Additional fluorine atoms are likely generated through dissociative recombination of NF_2^+. Neutral fluorine atoms are subsequently ionized by electron impact. The increased production of atomic fluorine would appear to be responsible for the higher concentrations of F^+ ions observed in 25 mol % NF_3/Ar plasmas (4%) and in 25 mol % NF_3/He plasmas (11%), as compared to F^+ concentrations observed in O_2 diluents (<2%) or in 50% C_2F_6/O_2 discharges (<0.5%). Higher concentrations of atomic and ionic fluorine contribute significantly to the faster etch rates in NF_3-based chamber cleaning plasmas compared to fluorocarbon plasmas.

2. Helium as the diluent for NF_3 discharge

When helium was used as the diluent at reactor pressure above 0.75 Torr, the pressure in the EQP probe could not be maintained below 5×10^{-6} Torr, which was required to ensure collisionless neutral streaming in the probe. This restricted our operating pressure range to be between 0.25 and 0.75 Torr for this gas mixture. The relative signal intensities measured for the principal positive ions incident on the grounded electrode in 25 mol % NF_3/He plasmas are shown in the second column of Fig. 2. Marked contrasts between helium- and argon-diluted plasmas are observed. First, He^+ constitutes only a small fraction of the total positive ion populations. With an ionization potential of 24.59 eV, helium atoms are much more difficult to ionize than argon atoms. The relatively low concentration of He^+ observed is consistent with previous plasma impedance measurements which showed NF_3/He plasmas to be more electronegative than NF_3/Ar plasmas.[5,6] We will discuss the effect of increased electronegativity on ion energy in Sec. III B.

NF_2^+ is one of the dominant ion species observed for 25 mol % NF_3/He discharges. He^+ has stored energy of 24.59 eV. The lowest metastable state of He^* ($1s2s\ ^3S_1$) has stored energy of 19.82 eV.[16] Therefore, both He^+ and He^* have sufficient energy to dissociatively ionize NF_3 to produce NF_2^+. In addition, He^* can dissociate NF_3 to produce NF_2,[17]

$$He^* + NF_3 \rightarrow NF_2 + F^* + He. \quad (2)$$

NF_2 has an ionization potential of 12.11 eV. Additional NF_2^+

can be produced by electron-impact ionization of NF_2 following reaction (2), or by subsequent interaction with He^+ or He^*. All of these reaction pathways diminish the populations of He^+ and He^*.

Helium ion and helium metastable driven NF_3 dissociation processes also produce fluorine atoms and ions in 25 mol % NF_3/He plasmas. Consequently, F_2^+ and F^+ constitute larger fractions of the total ion flux incident at the electrode, 12% and 11%, respectively. With lower mass, sheath-accelerated He^+ is not as effective as Ar^+ to activate SiO_2 or Si_3N_4 surfaces for reactive etching. Thus, the high fluxes of atomic and ionic fluorine are essential for maintaining high etch rates in helium-diluted NF_3 plasmas. Previous studies have demonstrated that Si_3N_4 etch rates in NF_3/He plasmas are close to those obtained in NF_3/Ar plasmas and much higher than those obtained in C_2F_6/O_2 and CF_4/O_2 plasmas.[5]

Another interesting feature of helium-diluted NF_3 discharges is the relatively high concentrations of N_2F^+ and N_2^+. Although masses 47 and 28 could also be from SiF^+ and Si^+, respectively, both isotope abundance analysis and OES analysis (see Sec. III C) support the assignment of N_2F^+ and N_2^+ to these masses, respectively. The presence of N_2F^+ and N_2^+ suggests that secondary reactions between fragmentation products in the gas phase and/or gas–surface interactions are more important in helium-diluted discharges. The presence of NO^+, see Fig. 2, may be a by-product of plasma–surface reactions. Alumina (Al_2O_3) is used in the reactor as an insulator. Oxygen, displaced when the alumina is subject to fluorine attack in the plasma, can then form NO^+ during secondary reactions with fragmentation products.

3. Oxygen as the diluent for NF_3 discharge

The third column in Fig. 2 shows the composition of the ion flux for 25 mol % NF_3 in O_2 plasmas. In contrast to inert diluent gases, O_2 has a relatively large dissociative electron capture cross section. Dilution with electron-attaching gases such as O_2 increases the electronegativity of NF_3 discharges. As a result, discharge above 0.75 Torr at 60 W rf power in 25 mol % NF_3 in O_2 plasmas could not be sustained.

In oxygen-diluted plasmas, a different set of molecular excitation, ionization, and dissociation pathways replaces the electron-driven inert gas reactions in the previous two types of plasmas. The ionization potential of O_2 (12.07 eV) is lower than that of NF_3 ($\sim$14 eV). Consequently, a large fraction of O_2^+ (28%) is detected, along with a smaller fraction of O^+ (5%). The most abundant ion is NO^+, which can be formed from secondary reactions between the daughter products of the feed gases. NO^+ can also be produced from ionization of NO, which is a stable molecule that can be formed in secondary reactions. With an ionization potential of 9.26 eV, NO can be readily ionized in the plasma. OES measurements from these discharges show progressions of NO emissions (see Sec. III C), corroborating our relative ion concentration measurements.

In sharp contrast to inert gas-diluted NF_3 plasmas, NF_2^+ makes up only a small fraction of the total positive ion flux when O_2 is used as the diluent. The relative fluxes of F_2^+ and F^+ in O_2-diluted NF_3 plasmas are also much smaller than those in inert gas-diluted NF_3 plasmas. With a lower ionization potential of 12.07 eV and with multiple rotational and vibrational excitation states, O_2 apparently acts as an energy sink inhibiting reactions which produce NF_x, NF_x^+, and neutral and ionic fluorine species. The much reduced relative fluorine fluxes observed here are consistent with previous measurements that etch rates in NF_3 plasmas diluted with O_2 are lower than those diluted with inert gases.

4. C_2F_6/O_2 plasmas

To compare with conventional fluorocarbon PECVD chamber cleaning recipes, we also measured the relative ion fluxes in 50 mol % C_2F_6 in O_2 plasmas. The results are plotted in column 4 of Fig. 2. A complex set of molecular reactions are manifested by a large variety of molecular ions. The incident flux on the electrode is principally composed of O_2^+ (56%). CF_3^+ is the next most abundant ion at 25% of the total flux. A multitude of other fluorocarbon and oxyfluorocarbon cations are also observed, each constituting, at most, 4% of the total flux. These observations are consistent with more extensive analysis of C_2F_6-based dielectric etch plasmas.[18]

Our ion measurements reveal two important features of 50 mol % C_2F_6 in O_2 plasmas. First, F^+ constitutes a very small fraction of the total ion flux ($<0.5\%$). The relative concentrations of F^+ or F_2^+ in C_2F_6-based plasmas are much less than those in any of the NF_3-based plasmas. These low concentrations explain the much lower etch rates observed in C_2F_6-based plasmas.[5] Second, it is also important to note the high abundance of CF_3^+ and other fluorocarbon cations in 50 mol % C_2F_6/O_2 plasmas. Cracking of C_2F_6 in the plasma produces perfluorocompounds (PFCs), such as CF_4, which absorb strongly in the infrared and adversely affect the earth's radiation balance, thus contributing to the greenhouse effect.[19]

B. Ion energy distribution functions (IEDFs)

In order to understand the plasma–tool surface interactions, we must characterize not only the relative concentrations of the ions, but also their energy distributions. For each ion energy distribution, we are concerned with two key characteristics: the average energy, which reflects the total energy deposition rate on the tool surfaces, and the intensity of the high-energy component of the incident flux, which affects sputtering rates. Figures 5(a)–5(d) show variations of IEDFs with pressure for one of the principal ions in each of the four plasmas investigated. Three general trends emerge from the data:

(1) the shapes of the IEDFs evolve from the bimodal structure to a single peak structure as the pressure increases;
(2) the average ion energies decrease and the IEDFs shift toward lower energies as the pressure increases; and
(3) the IEDFs shift toward lower energies as the electronegativity of the discharge increases.

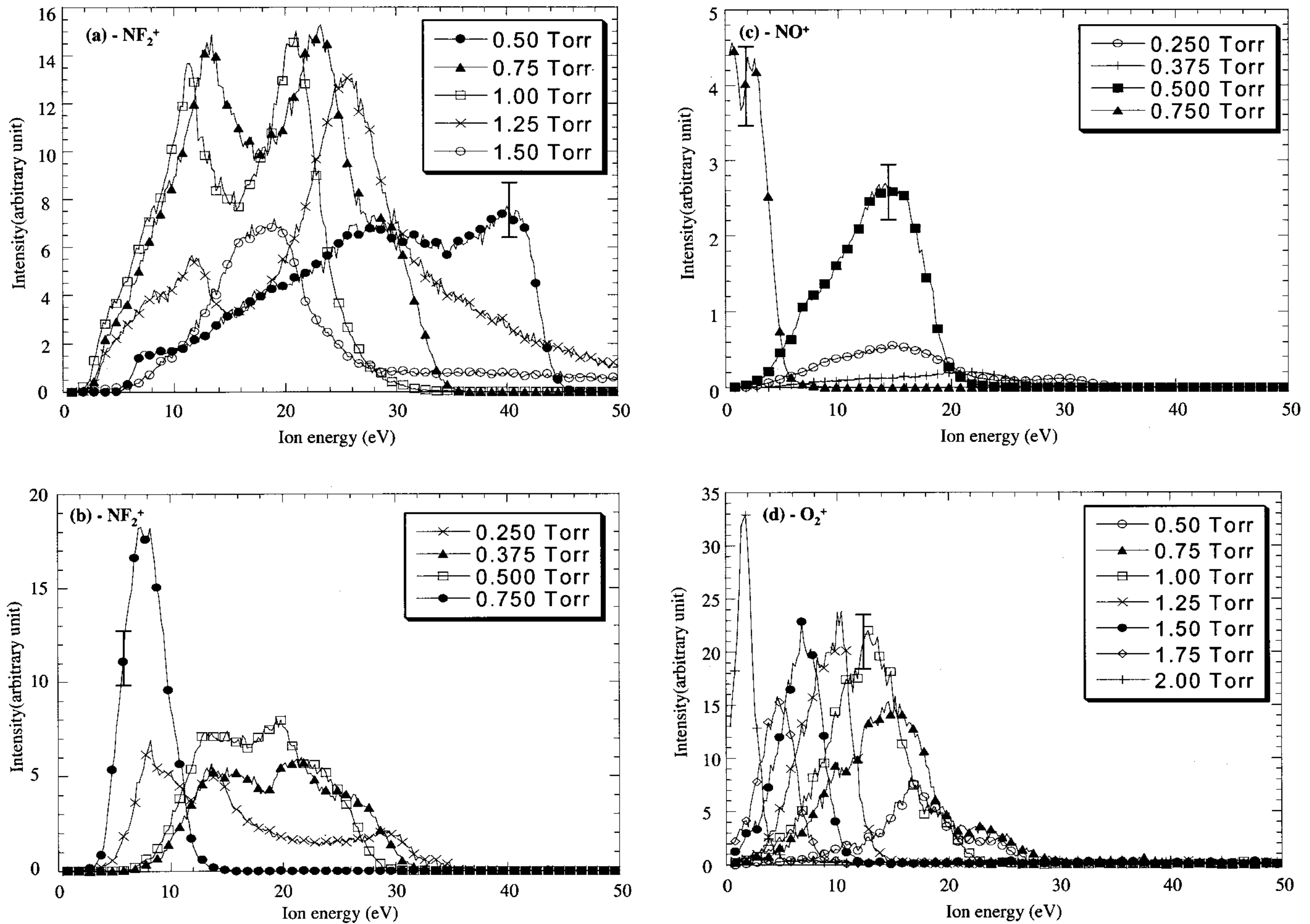

FIG. 5. Ion energy distribution function variation with pressure for one of the principal ions in the plasmas: (a) NF_2^+ in 25 mol % NF_3 in Ar; (b) NF_2^+ in 25 mol % NF_3 in He; (c) NO^+ in 25 mol % NF_3 in O_2; and (d) O_2^+ in 50 mol % C_2F_6 in O_2. Data were taken every 0.2 eV. The accuracy of the energy measurement provided by the Hiden EQP probe is ±0.5 eV. Error bars shown the results from repeated measurements made on different days and largely reflect the variability of the process chamber conditioning, which is often referred to in the industrial community as chamber drift.

Similar behaviors have also been observed in capacitively coupled Ar and SF_6 plasmas.[20–22] All three trends are manifestations of changes in plasma impedance, and we can correlate the trends observed here with plasma impedance measurements in previous studies of NF_3-based plasmas.[5–7] To facilitate our analysis, we outline three fundamental physical processes as pressure and electronegativity change.

(1) Previous studies[5–7] of 25 mol % NF_3/Ar plasmas have shown that as the pressure increases, the plasma impedance changes from a sheath-dominated, more capacitive regime to a bulk plasma-dominated, more resistive regime. As the pressure increases, the ions experience more collisions in the sheath. This increase in collision rate hinders the acceleration of ions across the sheath, resulting in increased ion charge density in the sheath, which, in turn, reduces sheath width s and sheath impedance Z_s. Sheath models[23] have shown $Z_s \propto p^{-1/2}$, where p is the pressure. The bulk plasma impedance, on the other hand, has an opposite dependence on pressure. In the bulk, higher pressure induces more frequent electron collisions, resulting in higher resistance R_b. In fact, $|Z_b| \approx R_b \propto v_e \propto p$, where v_e is electron collision frequency. Since the rf driving voltage is divided across the powered electrode sheath, the bulk plasma, and the grounded electrode sheath, decreasing sheath impedance Z_s and increasing bulk resistance R_b as pressure increases, leads to increased bulk rf voltage $\tilde{V}_b$ and decrease of sheath rf voltage $\tilde{V}_s$. Such changes in $\tilde{V}_b$ and $\tilde{V}_s$ as a function of pressure have been observed experimentally in 25 mol % NF_3/Ar,[6,7] as well as other plasmas.[18–28] In addition, the decrease (or constriction) of sheath width s as pressure increases has been directly observed by spatially resolved OES.[26–29]

(2) At higher pressure, the inelastic electron-heavy particle collision rate increases, leading to a decrease in electron temperature T_e.[30] Lower T_e leads to lower rate of high-energy electrons escaping to the reactor wall. In other words, there is less positive space charge in the plasma at lower T_e. This in turn leads to lower plasma potential V_p.[31] Since the dc voltage drop across the grounded electrode sheath $\bar{V}_s = V_p$, $\bar{V}_s$ also decreases as pressure increases. Decrease of electron temperature T_e with increasing pressure has also been confirmed by our OES analysis, as discussed in Sec. III C.

(3) At fixed power, the electron density n_e decreases as

plasma electronegativity increases. Since bulk plasma resistance is inversely proportional to electron density, $R_b \propto n_e^{-1}$, increased electronegativity also leads to an increased bulk plasma resistance and corresponding decreases in both rf sheath voltage $\tilde{V}_s$,[6] and in plasma potential V_p.[22] Thus, at a fixed power density, increased electronegativity can lower the energy spectra of ions impinging upon the electrodes. Note that a similar reduction in incident ion energies can be achieved by raising the pressure so as to increase ion collisions in the sheath. In the results presented below, the effects of both increased electronegativity and of increased pressure are observable.

These fundamental physical processes provide the guideline for us to understand the IEDFs observed in this study. The decrease of average ion energy and the downward shift of IEDFs with the increase of pressure and/or electronegativity, as noted in general trends (2) and (3) above, are the direct consequences of decreasing sheath impedance Z_s, increasing bulk plasma resistance R_b, and decreasing plasma potential V_p, as outlined in processes (2) and (3) above.

To understand changes in the shapes of the IEDFs, we need to understand the dynamics of the ion transport processes across the sheath. Extensive sheath modeling studies[23–25,32–38] under various conditions provide the insights into these ion transport processes. A recent review article by Kawamura *et al.*[38] gives a heuristic and comprehensive overview of the subject. For the low-frequency, collisionless regime ($\tau_{\text{ion}} \ll \tau_{\text{rf}}$, where τ_{ion} is the ion transient time across the sheath, and τ_{rf} is the rf cycle time), the ions cross the sheath in a small fraction of a rf cycle and respond to instantaneous rf sheath voltage $\tilde{V}_s$. This leads to the double-humped, bimodal structure for the IEDF reported by Woodworth *et al.* and others,[39,40] where the two peaks in the IEDF correspond to the maximum and the minimum in the rf sheath voltage.

In the high-frequency, collisionless regime ($\tau_{\text{ion}} \gg \tau_{\text{rf}}$), the effect of rf sheath voltage $\tilde{V}_s$ is confounded by averaging over several rf cycles. Assuming a Child–Langmuir space-charge sheath electric field, and the sheath voltage

$$V_s(t) = \bar{V}_s + \tilde{V}_s \sin \omega t, \tag{3}$$

where $\bar{V}_s$ is the dc sheath voltage, $\tilde{V}_s$ is the amplitude of the rf sheath voltage, and $\omega = 2\pi f$, Benoit-Cattin and Bernard[32] and Kawamura *et al.*[38] have derived the following form for the IEDF:

$$f(E) = \frac{dn}{dE} = \frac{2n_t}{\omega \Delta E}\left[1 - \frac{4}{\Delta E^2}(E - e\bar{V}_s)^2\right] \tag{4}$$

and

$$\Delta E = \frac{8e\tilde{V}_s}{3\bar{s}\omega}\left(\frac{2e\bar{V}_s}{M}\right)^{1/2} = \frac{4e\tilde{V}_s}{\pi}\left(\frac{\tau_{\text{rf}}}{\tau_{\text{ion}}}\right), \tag{5}$$

where n_t is the number of ions entering the sheath per unit time, and $\bar{s}$ is the time-averaged sheath width. Equation (4) predicts a double-humped, bimodal IEDF with two peaks symmetric about $e\bar{V}_s$ and the separation ΔE given by Eq. (5). The second part of Eq. (5) shows that ΔE depends on *both* the ion transient time τ_{ion} (or $\tau_{\text{rf}}/\tau_{\text{ion}}$) *and* the amplitude of the rf sheath voltage $\tilde{V}_s$. The double-humped, bimodal IEDFs observed at lower pressures in NF_3/Ar and NF_3/He discharges implies that a fully collisional sheath has not developed in these cases.

Even though Eq. (5) represents a collisionless description, it serves well as a starting point for understanding the evolution of the IEDF shapes observed in the collisional plasmas studied here. As outlined in the fundamental processes above, increasing pressure and/or increasing electronegativity leads to decreasing of $\tilde{V}_s$, $\bar{V}_s$, and $\bar{s}$. The effect of decreasing $\tilde{V}_s$ and $\bar{V}_s$ dominates the effect of decreasing $\bar{s}$, decreasing of ΔE as pressure and/or electronegativity increases. Coupled with decreasing ion energies as a result of collisions in the sheath, we find that IEDFs evolve from double-humped, bimodal shapes to single-peak unimodal shapes as pressure and/or electronegativity increase. This general trend is observed in our data. We note that the high-energy portion of the IEDF in 25 mol % NF_3/Ar at 1.25 Torr represents an exception to the general trend. This may result from an anomaly in the extensive tuning procedure required at each pressure and each gas mixture for measurement of IEDFs at each ion mass.

As shown in Figs. 5(a)–5(d), ion energies observed in 25 mol % NF_3/He and in 25 mol % NF_3/O_2 plasmas are much lower than those in 25% NF_3/Ar plasmas. In addition, the IEDFs in 25 mol % NF_3/He and in 25 mol % NF_3/O_2 plasmas are comparable to those in 50 mol % C_2F_6/O_2 plasmas. The results show that proper choice of diluent gas and pressure can significantly lower the ion energies in NF_3-based plasmas. Corresponding electrode damage levels then should be comparable to those obtainable with C_2F_6-based cleaning plasmas.

One objective of this study was to identify mechanisms to reduce or to eliminate the flux of higher-energy (above, say, 15 eV) ions incident at the reactor electrodes while simultaneously maintaining an acceptable etch rate. Figures 5(b) and 5(c) show that this can be accomplished with NF_3 discharges diluted with either He or O_2 operated at relatively high pressures, $p \geq 0.75$ Torr. Figure 5(d) shows that comparably ''soft'' IEDFs can also be produced in 50 mol % fraction C_2F_6/O_2 discharges if operated at slightly higher pressures of 1.5–2.0 Torr.

As discussed above, electronegativity increases progressively through Figs. 5(a)–5(d) as energy partition pathways change and as more negative ion forming molecules (O_2) are added. Both negative ion formation and increased sheath collisionality, resulting from increased pressure, drive the IEDF toward lower energies. For highly collisional, high-pressure electronegative discharges with relatively small sheath potential drops, Figs. 5(c) and 5(d), nearly Gaussian IEDFs peaked near zero energy are obtained. Thus, loss of discrimination for low-energy ions does not appear to be a problem even for fluorocarbon discharges which have the potential for surface charge buildup on the EQP's collection orifice.

The IEDFs in this work are for ions incident upon the grounded electrode surface. IEDFs at the powered electrode

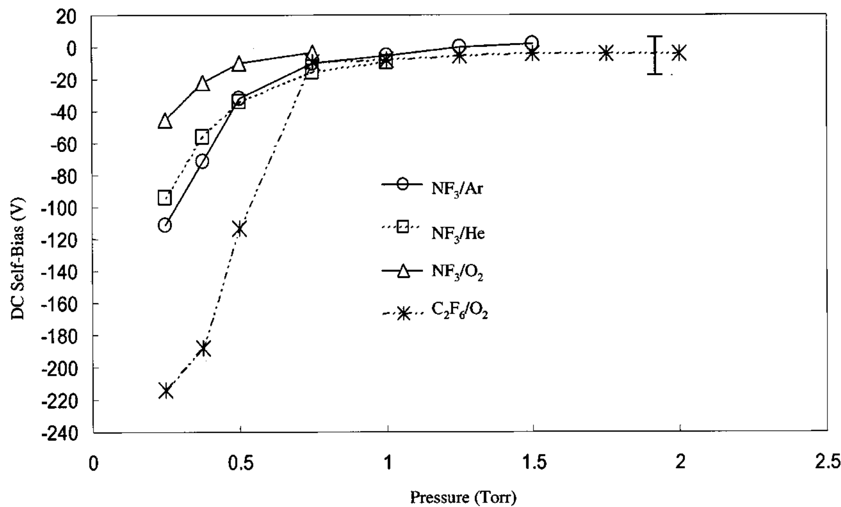

FIG. 6. DC self-bias of the powered electrode in the plasmas. Error bars on all data points are ±5 V, as shown for the data points at 1.75 Torr.

surface also depend on the dc self-bias and the rf voltage across the powered electrode sheath. Figure 6 is a plot of the dc self-bias as a function of reactor pressure in the four plasmas. In general, the more electronegative the discharge, the less negative the dc bias. As shown in Fig. 6, increasing reactor pressure makes the dc bias less negative, hence, reducing the energy of the ions traversing the powered electrode sheath. We can thus infer that conditions that minimize the ion energy at the ground electrode surface can also reduce the ion energy at the powered electrode surface.

As was pointed out in Sec. III A above, 25 mol % NF_3/He plasmas provide higher concentrations of atomic and ionic fluorine species, and have much higher etch rates than C_2F_6, or CF_4-based plasmas. At the same time, NF_3/He plasmas produce much lower ion energies and, consequently, less damage to electrode surfaces than do NF_3/Ar plasmas. Combined with previous etch rate optimization studies, the ion concentration and ion energy measurements presented here show that NF_3/He plasmas operated at higher pressures can be used to minimize PECVD chamber cleaning times, and at the same time, reduce ion bombardment damage of hardware surfaces.

C. Optical emission spectroscopy (OES)

Optical emission spectroscopy (OES) is a low cost and easy to implement diagnostic technique. OES data can corroborate and complement the results of other diagnostic measurements, such as mass spectrometry. Furthermore, changes in the OES data can be correlated to the trends observed in ion energy measurements. Figures 7(a)–7(d) show the OES of the four plasmas investigated in this work. All OES were taken at the same time with the ion measurements.

1. Identification of the atomic and molecular species in the plasmas

Prominent atomic fluorine, argon, helium, and oxygen lines are readily identified in the OES. Analysis of these atomic emissions will be presented in the following subsections. We identify other emitting species here to corroborate our earlier relative ion concentration analysis. In all three NF_3-based plasmas, the bands in the N_2 second positive system $(C\,^3\Pi_u - B\,^3\Pi_g)$[41,42] are readily observed.

In 25 mol % NF_3/He plasmas [Fig. 7(b)], some vibrational bands of the N_2^+ first negative system $(B\,^2\Sigma_u^+ - X\,^2\Sigma_g^+)$ are observed in addition to N_2 bands. On the other hand, the characteristic Si 288.2 nm line and the SiF α system $(A\,^2\Sigma^+ - X\,^2\Pi)$[41,42] between 430 and 450 nm are not observed in the OES. Therefore, the OES data corroborate the finding of relatively higher concentrations of N_2^+ and N_2F^+ in 25 mol % NF_3/He plasmas measured by the EQP mass spectrometer. Since there was no wafer in the reactor, the absence of Si and SiF_x species suggests that etching of the quartz windows of the reactor is not a serious problem.

In 25 mol % NF_3/O_2 plasmas [Fig. 7(c)], the NO γ system $(A\,^2\Sigma^+ - X\,^2\Pi)$[41,42] between 220 and 300 nm is observed. Some NO β systems $(B\,^2\Pi - X\,^2\Pi)$[41,42] are also clearly observed. While NO can be a strong emitter under favorable conditions, the NO emission observed in NF_3/O_2 plasma is quite weak compared to other emitting species. This implies that neutral NO concentration is limited by ionization and secondary reaction processes, such as NO $+F \rightarrow$NOF, etc. The NO optical emission supports our ion measurement finding that secondary reactions between the dissociation fragments are important chemical reaction pathways in 25 mol % NF_3/O_2 plasmas. This also suggests that ionization of NO is a viable pathway to produce NO^+, as we have discussed in ion concentration analysis. Another prominent feature here is the O_2^+ first negative system $(b\,^4\Sigma_g^- - a\,^4\Pi_u)$.[41,42] Bands in the O_2^+ first negative system are complex, and cannot be fully resolved in our spectrum. Nevertheless, we can identify the overlapped (7,5), (6,4), (5,3), (4,2), (3,1), and (2,0) bands centered around 526 nm, the (2,1) and (1,0) bands centered around 560 nm, and the (1,1) and (0,0) bands centered around 600 nm. This confirms our finding that O_2^+ is one of the most abundant ions in the plasma.

The most prominent molecular emission in the 50 mol % C_2F_6/O_2 plasma [Fig. 6(d)] is the CO angstrom system $(B\,^1\Sigma^+ - A\,^1\Pi)$.[41,42] The C_2F_6/O_2 plasma OES has con-

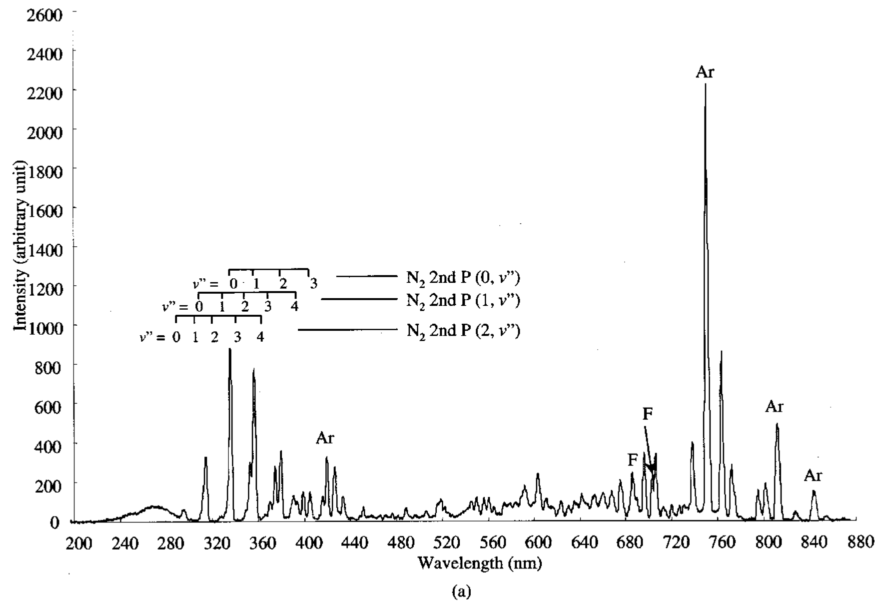

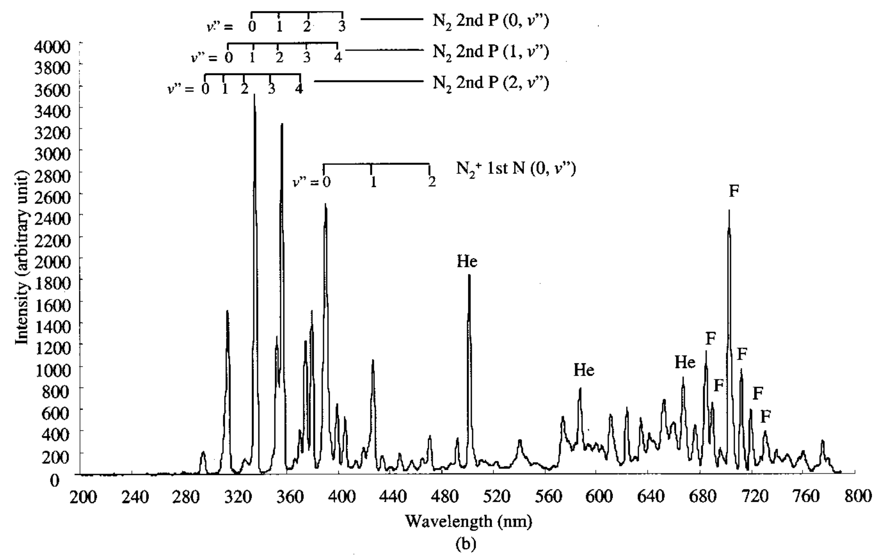

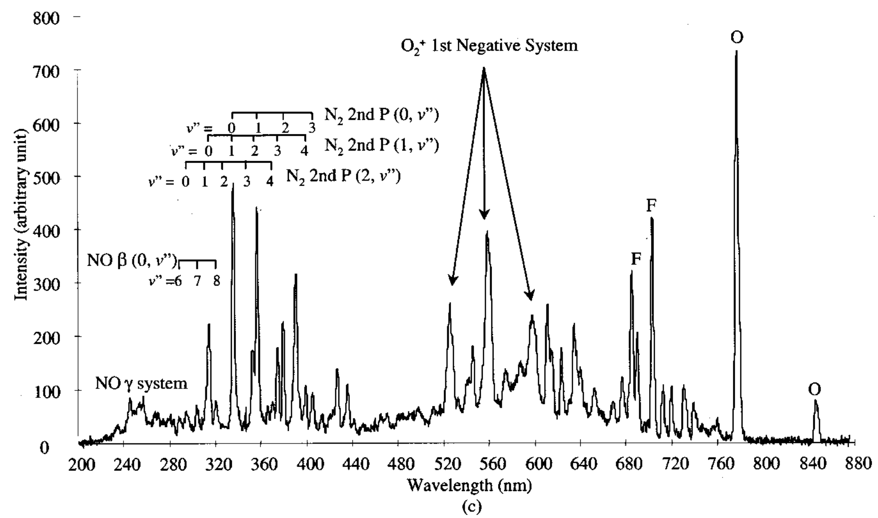

FIG. 7. Optical emission spectra for each plasma: (a) 25 mol % NF_3 in Ar; (b) 25 mol % NF_3 in He; (c) 25 mol % NF_3 in O_2; and (d) 50 mol % C_2F_6 in O_2.

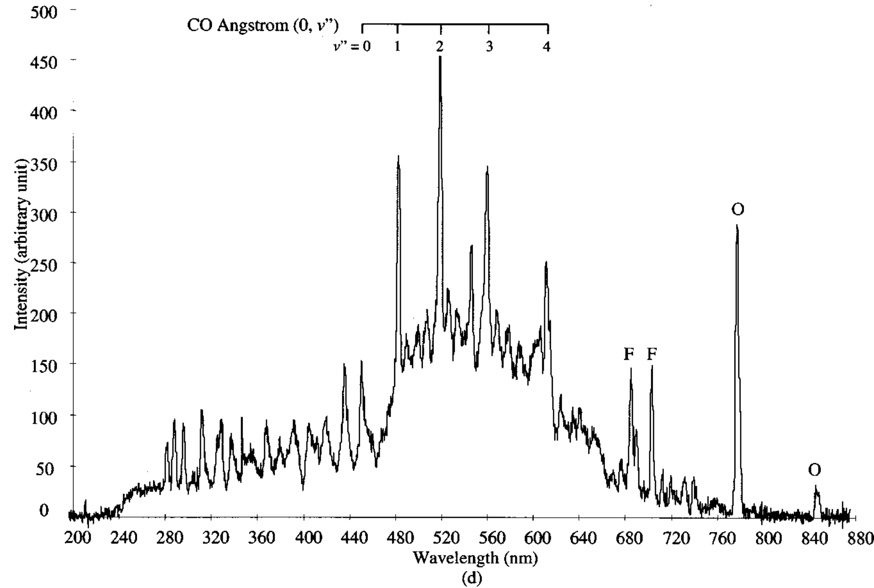

FIG. 7. (*Continued.*)

gested bands and continuous background, indicating complex neutral and ionic species in the plasma.

2. Estimate of atomic fluorine densities by actinometry

Table I lists some prominent atomic fluorine, argon, and helium emission lines observed in our OES. Data in Table I are taken from the NIST Atomic Spectroscopic Database.[43] The Grotrian diagrams for the selected atomic energy levels and transition wavelengths are also plotted in Fig. 4. Coburn and Chen[44] first applied actinometry to determine atomic fluorine density n_{F} by

$$n_{\mathrm{F}} \propto n_{\mathrm{Ar}} I_{\mathrm{F}(704)} / I_{\mathrm{Ar}(750)}, \tag{6}$$

where n_{Ar} is the atomic argon density, $I_{\mathrm{F}(704)}$ is the OES intensity of atomic fluorine transition $2s^2 2p^4(^3P)3p\ ^2P^{\circ}_{3/2} \rightarrow 2s^2 2p^4(^3P)3s\ ^2P_{3/2}$ at 703.75 nm, and $I_{\mathrm{Ar}(750)}$ is the OES intensity of atomic argon transition $3s^2 3p^5 \times(^2P^{\circ}_{1/2})4p\ ^2[1/2]_0 \rightarrow 3s^2 3p^5(^2P^{\circ}_{1/2})4s\ ^2[1/2]^{\circ}_1$ at 750.39 nm. Actinometry Eq. (6) assumes both $I_{\mathrm{F}(704)}$ and $I_{\mathrm{Ar}(750)}$ transitions arise from electron-impact excitation of ground electronic state atoms, and that the cross sections for both processes have similar energy dependence. Coburn and Chen used a small percentage (1%–2%) of argon in CF_4/O_2 plasmas so as not to perturb the CF_4/O_2 plasma that they investigated. Later, Donnelly *et al.* verified the validity of the actinometry Eq. (6) in NF_3/Ar plasmas over a wide argon mole fraction range (4%–95%) at 0.35 Torr.[10] Donnelly *et al.* showed excellent agreement between fluorine densities determined by actinometry and fluorine densities determined by downstream chemiluminescent titration reaction of fluorine atoms with added Cl_2.

Adopting the same approach, we calculated the atomic fluorine densities in NF_3/Ar plasmas normalized to 1 Torr. The results are shown in Fig. 8. We also plotted in Fig. 8 the normalized Si_3N_4 etch rates determined by previous studies.[5] The correlation between atomic fluorine density and etch rate is evident. This is consistent with our ion concentration analysis. Increasing pressure enhances fluorine production and, hence, increases etch rate.

Despite the direct experimental verification by Donnelly *et al.* and by the unequivocal correlation shown in Fig. 8, there may be some lingering concerns over the applicability of the actinometry Eq. (6) to large argon mole fractions: radiation trapping may distort $I_{\mathrm{Ar}(750)}$ intensity measurement, and metastable argon atoms may be excited into the upper state $[3s^2 3p^5(^2P^{\circ}_{1/2})4p\ ^2[1/2]_0]$, hence, contributing to $I_{\mathrm{Ar}(750)}$. To address these concerns, some further discussion is warranted here.

(1) The lower state of the argon $I_{\mathrm{Ar}(750)}$ transition, $3s^2 3p^5(^2P^{\circ}_{1/2})4s\ ^2[1/2]^{\circ}_1$, has a radiation lifetime of only 2

TABLE I. Selected atomic transitions in NF_3-based chamber cleaning plasmas.

Atom	Wavelength (nm)	Upper state (k)	E_k (eV)	Lower state (i)	E_i (eV)
Ar I	420.07	$3s^2 3p^5(^2P^{\circ}_{3/2})5p\ ^2[5/2]_3$	14.50	$3s^2 3p^5(^2P^{\circ}_{3/2})4s\ ^2[3/2]^{\circ}_2$	11.55
Ar I	750.39	$3s^2 3p^5(^2P^{\circ}_{1/2})4p\ ^2[1/2]_0$	13.48	$3s^2 3p^5(^2P^{\circ}_{1/2})4s\ ^2[1/2]^{\circ}_1$	11.83
He I	587.56	$1s3d\ ^3D_1$	23.07	$1s2p\ ^3P^{\circ}_1$	20.96
F I	703.75	$2s^2 2p^4(^3P)3p\ ^2P^{\circ}_{3/2}$	14.75	$2s^2 2p^4(^3P)3s\ ^2P_{3/2}$	12.99
O I	777.42	$2s^2 2p^3(^4S^{\circ})3p\ ^5P_2$	10.74	$2s^2 2p^3(^4S^{\circ})3s\ ^5S^{\circ}_2$	9.15

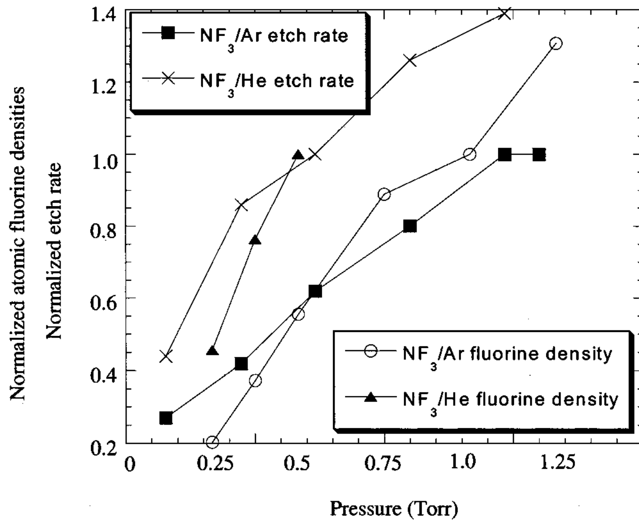

FIG. 8. Normalized atomic fluorine densities determined by actinometry compared to relative etch rates. Atomic fluorine density was normalized to the values at 1 Torr for 25 mol % NF_3 in Ar and to 0.5 Torr for 25 mol % NF_3 in He. Si_3N_4 etch rates for these two discharge compositions were normalized to etch rate values at 1.1 and 0.5 Torr, respectively.

ns.[16] The frequency of the transition from the $3s^23p^5(^2P^\circ_{1/2})4s\ ^2[1/2]^\circ_1$ state to the ground state is several times higher than those of the transitions from higher-energy states to the $3s^23p^5(^2P^\circ_{1/2})4s\ ^2[1/2]^\circ_1$ state. Since the Einstein coefficients A_{ik} for spontaneous emission are proportional to the third power of the transition frequencies, the rate coefficient of depopulating the $3s^23p^5(^2P^\circ_{1/2})4s\ ^2[1/2]^\circ_1$ state by spontaneous emission is faster than the rate coefficient of populating the state by spontaneous emission from higher-energy states above it. Steady-state population of the $3s^23p^5(^2P^\circ_{1/2})4s\ ^2[1/2]^\circ_1$ state cannot be maintained by radiation pumping. At 11.83 eV above ground, thermal excitation contributes negligibly to the $3s^23p^5(^2P^\circ_{1/2})4s\ ^2[1/2]^\circ_1$ state population. Therefore, we conclude that there are not enough atoms in the $3s^23p^5(^2P^\circ_{1/2})4s\ ^2[1/2]^\circ_1$ state to cause radiation trapping even with pure argon at a few Torr pressure.

(2) By analyzing optical emission spectral line shapes, Gottscho and Donnelly[45] have shown that both Ar* and F* in CF_4/O_2/Ar plasmas are created by electron-impact excitation of ground-state atoms, hence, actinometry is valid. In addition, the minor effect of metastable state excitation can be at least partially canceled out by normalizing n_F measured at different pressures. The normalized (i.e., relative) atomic fluorine density is plotted in Fig. 8.

In summary, we believe actinometry Eq. (6) can be reasonably applied to plasmas with large argon fractions,[46,47] as has been experimentally confirmed by Donnelley *et al.*

For 25 mol % NF_3/He plasma, we used the ratio of $I_{F(704)}/I_{He(588)}$ to estimate atomic fluorine density. The estimated fluorine densities are normalized to the density at 0.5 Torr. The results are also plotted in Fig. 8, along with normalized etch rates in 25% NF_3/He plasmas from the previous study. The use of actinometry with $I_{F(704)}/I_{He(588)}$ in NF_3/He plasmas does indeed have complications. As pointed out in Sec. III A, metastable states He* have enough energy to dissociate NF_3 and produce excited state F* through processes such as Eq. (2). In fact, Eq. (2) has been proposed as a possible cause of the anomalously high fluorine OES intensities in NF_3/He plasmas.[17] The anomalously high fluorine OES intensities can lead to overestimated atomic fluorine densities using the $I_{F(704)}/I_{He(588)}$ ratio. However, by normalizing fluorine densities to that at 0.5 Torr, the effect of He* is partially canceled out. Hence, we observe the trend of increasing *relative* atomic fluorine density in 25 mol % NF_3/He plasmas as pressure increases. Similar to NF_3/Ar plasmas, increasing atomic fluorine density also correlates to the etch rate increase in NF_3/He plasmas.

3. Correlation of argon OES intensity ratio to plasma electron temperature

Donnelly and his colleagues have developed trace rare-gas optical emission spectroscopy (TRG-OES) in Cl_2-based etch plasmas.[48–51] Small percentages of each of the five rare gases are introduced into the plasma. By fitting all the rare-gas OES line intensities, Donnelly *et al.* were able to determine the electron temperature T_e and the electron energy distribution function (EEDF). Guided by their approach, we seek to ascertain qualitative trends in T_e from argon OES line intensities in 25 mol % NF_3/Ar plasmas without adding other rare gases.

The argon $3s^23p^5(^2P^\circ_{3/2})5p\ ^2[5/2]_3 \rightarrow 3s^23p^5(^2P^\circ_{3/2})4s\ ^2[3/2]^\circ_1$ transition at 420.07 nm originates from an upper state of 14.50 eV. This is 1.02 eV higher in excitation energy than 13.48 eV for the 750.39 nm transition. When the plasma electron temperature T_e decreases, the number of electrons with $E > 14.50$ eV decreases more rapidly than the number of electrons with $E > 13.48$ eV. Consequently, the electron-impact excitation for the 420.07 nm transition is suppressed more than that for the 750.39 nm transition when T_e decreases. This means that the ratio of the OES intensities at 420.07 and 750.39 nm, $I_{Ar(420)}/I_{Ar(750)}$, decreases as T_e decreases.

Figure 9 is a plot of fractional decrease of $I_{Ar(420)}/I_{Ar(750)}$ as a function of pressure in 25 mol % NF_3/Ar plasmas. Also shown in Fig. 9 is the fractional change in the dc sheath voltage $\bar{V}_s$ at the grounded electrode, which we determine as the mean energy between the double peaks of the bimodal IEDFs for NF_2^+ plotted in Fig. 5(a), or as the peak energy for unimodal IEDFs.[38] As we discussed in Sec. III B, increasing pressure leads to decreased T_e. Decreased T_e leads to lower plasma potential and, consequently, decreased mean ion energies at the grounded electrode. Therefore, by monitoring changes in the OES intensity ratio $I_{Ar(420)}/I_{Ar(750)}$, we can infer changes in the mean energy of ions incident onto the hardware interior surfaces. Given the low cost and easy implementation of the OES on commercial plasma processing tools, the correlation between $I_{Ar(420)}/I_{Ar(750)}$ and E_{avg} established in this study provides a powerful practical tool for ion energy optimization in NF_3-based chamber cleaning plasmas.

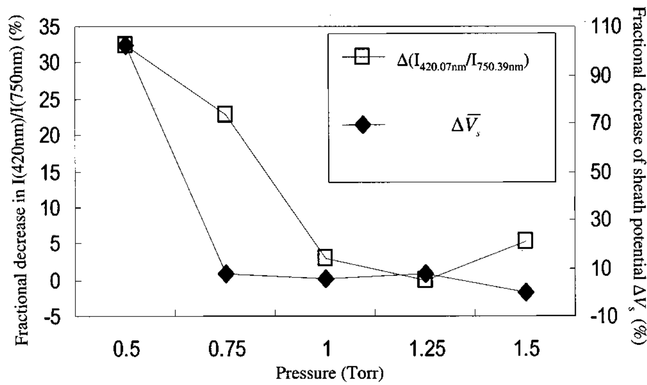

FIG. 9. Correlation between (a) the fractional change in ratio of Ar emission lines from the $3s^2 3p^5(^2P^{\circ}_{3/2})5p\ ^2[5/2]_3$ state at 14.50 eV above ground and the $3s^2 3p^5(^2P^{\circ}_{1/2})4p\ ^2[1/2]_0$ state at 13.48 eV above ground, $(I_{\mathrm{Ar}(420)}/I_{\mathrm{Ar}(750)})$, and (b) the fractional change in average ground sheath potential as measured through ion energy distributions, $\Delta \bar{V}_s$.

IV. CONCLUSION

We have demonstrated that proper selection of diluent gases (such as helium) and optimization of operation conditions (such as higher pressure) can effectively reduce the ion bombardment energies in NF_3-based chamber cleaning plasmas without adversely affecting SiO_2 and Si_3N_4 etch rates. We have established the correlation between the argon OES intensity ratio $I_{\mathrm{Ar}(420)}/I_{\mathrm{Ar}(750)}$ and the average energy of ions incident upon hardware surfaces. This correlation will help us to further optimize NF_3-based chamber cleaning plasmas.

ACKNOWLEDGMENT

This work was supported by Air Products and Chemicals, Inc.

[1]B. Golja, J. A. Barkanic, and A. Hoff, Microelectron. J. **16**, 5 (1985).
[2]J. A. Barkanic, D. M. Reynolds, R. J. Jaccodine, H. Stenger, J. Parks, and H. L. Vedage, Solid State Technol. **32**, 109 (1989).
[3]P. Maroulis, J. Langan, A. Johnson, R. Ridgeway, and H. Withers, Semicond. Int. **17**, 107 (1994).
[4]J. Langan, P. Maroulis, and R. Ridgeway, Solid State Technol. **39**, 115 (1996).
[5]J. G. Langan, S. E. Beck, B. S. Felker, and S. W. Rynders, J. Appl. Phys. **79**, 3886 (1996).
[6]M. A. Sobolewski, J. G. Langan, and B. S. Felker, J. Vac. Sci. Technol. B **16**, 173 (1998).
[7]J. G. Langan, S. W. Rynders, B. S. Felker, and S. E. Beck, J. Vac. Sci. Technol. A **16**, 2108 (1998).
[8]W. R. Entley, J. G. Langan, B. S. Felker, and M. A. Sobolewski, J. Appl. Phys. **86**, 4825 (1999).
[9]K. M. Eisele, Proceedings of the 3rd Symposium on Plasma Processing, Vol. 82, p. 146 (1982).
[10]V. M. Donnelly, D. L. Flamm, W. C. Dautremont-Smith, and D. J. Werder, J. Appl. Phys. **55**, 242 (1984).
[11]M. V. V. S. Rao, R. J. Van Brunt, and J. K. Olthoff, Phys. Rev. E **54**, 5641 (1996).
[12]Y. Wang and J. K. Olthoff, J. Appl. Phys. **85**, 6358 (1999), and private communications.
[13]V. Tarnovsky, A. Levin, K. Becker, R. Basner, and M. Schmidt, Int. J. Mass Spectrom. Ion Processes **133**, 175 (1994).
[14]R. M. Reese and V. H. Dibeler, J. Chem. Phys. **24**, 1175 (1956).
[15]T. M. Miller, J. F. Friedman, A. E. Stevens Miller, and J. F. Paulso, J. Phys. Chem. **98**, 6144 (1994).
[16]A. A. Radzig and B. M. Smirnov, *Reference Data on Atoms, Molecules, and Ions* (Springer, Berlin, 1985).
[17]T. Honda and W. W. Brandt, J. Electrochem. Soc. **131**, 2667 (1984).
[18]R. Jayaraman, R. T. McGrath, and G. A. Hebner, J. Vac. Sci. Technol. A **17**, 1545 (1999).
[19]S. Raoux, T. Tanaka, M. Bhan, H. Ponnekanti, M. Seamons, T. Deacon, L.-Q. Xia, F. Pham, D. Silvetti, D. Cheung, K. Fairbairn, A. Johnson, R. Pearce, and J. Langan, J. Vac. Sci. Technol. B **17**, 477 (1999).
[20]J. K. Olthoff, R. J. Van Brunt, and S. B. Radovanov, J. Appl. Phys. **72**, 4566 (1992).
[21]J. K. Olthoff, R. J. Van Brunt, S. B. Radovanov, J. A. Rees, and R. Surowiec, J. Appl. Phys. **75**, 115 (1994).
[22]R. Foest, J. K. Olthoff, R. J. Van Brunt, E. C. Benck, and J. R. Roberts, Phys. Rev. E **54**, 1876 (1996).
[23]M. A. Lieberman, IEEE Trans. Plasma Sci. **17**, 338 (1989).
[24]V. A. Godyak and N. Sternberg, Phys. Rev. A **42**, 2299 (1990).
[25]M. A. Sobolewski, Phys. Rev. E **56**, 1001 (1997).
[26]P. Bletzinger and C. A. DeJoseph, Jr., IEEE Trans. Plasma Sci. **PS-14**, 124 (1986).
[27]P. Bletzinger, J. Appl. Phys. **67**, 130 (1990).
[28]S. B. Radovanov, B. Tomcik, Z. Lj. Petrovic, and B. M. Jelenkovic, J. Appl. Phys. **67**, 97 (1990).
[29]Z. Lj. Petrovic, F. Tochikubo, S. Kakuta, and T. Makabe, J. Appl. Phys. **73**, 2163 (1993).
[30]M. A. Lieberman and A. J. Lichtenberg, *Principles of Plasma Discharges and Materials Processing* (Wiley, New York, 1994).
[31]A. Schwabedissen, E. C. Benck, and J. R. Roberts, Phys. Rev. E **55**, 3450 (1997).
[32]P. Benoit-Cattin and L. C. Bernard, J. Appl. Phys. **39**, 5723 (1968).
[33]R. T. C. Tsui, Phys. Rev. **168**, 107 (1968).
[34]M. J. Kushner, J. Appl. Phys. **58**, 4024 (1985).
[35]B. E. Thompson, H. H. Sawin, and D. Fischer, J. Appl. Phys. **63**, 2241 (1988).
[36]J. Liu, G. L. Huppert, and H. H. Sawin, J. Appl. Phys. **68**, 3916 (1990).
[37]P. A. Miller and M. E. Riley, J. Appl. Phys. **82**, 3689 (1997).
[38]E. Kawamura, V. Vahedi, M. A. Lieberman, and C. K. Birdsall, Plasma Sources Sci. Technol. **8**, R45 (1999).
[39]J. R. Woodworth, M. E. Riley, D. C. Meister, B. P. Aragon, M. S. Le, and H. H. Sawin, J. Appl. Phys. **80**, 1304 (1996).
[40]M. A. Sobolewski, J. K. Olthoff, and Y. Wang, J. Appl. Phys. **85**, 3966 (1999).
[41]G. Herzberg, *Molecular Spectra and Molecular Structure*, 2nd ed. (Krieger, Malabar, FL, 1989), Vol. I.
[42]K. P. Huber and G. Herzberg, *Molecular Spectra and Molecular Structure* (Van Nostrand Reinhold, New York, 1979).
[43]NIST Atomic Spectroscopic Database, U.S. Department of Commerce, National Institute of Standards and Technology, Gaithersburg, MD (1999).
[44]J. W. Coburn and M. Chen, J. Appl. Phys. **51**, 3134 (1980).
[45]R. A. Gottscho and V. M. Donnelly, J. Appl. Phys. **56**, 245 (1984).
[46]G. S. Selwyn (private communication).
[47]M. V. Malyshev (private communication).
[48]V. M. Donnelly, J. Vac. Sci. Technol. A **14**, 1076 (1996).
[49]M. V. Malyshev and V. M. Donnelly, J. Vac. Sci. Technol. A **15**, 550 (1997).
[50]M. V. Malyshev, V. M. Donnelly, and S. Samukawa, J. Appl. Phys. **84**, 1222 (1998).
[51]V. M. Donnelly, M. V. Malyshev, A. Kornblit, N. A. Ciampa, J. I. Colonell, and J. T. C. Lee, Jpn. J. Appl. Phys., Part 1 **37**, 2388 (1998).